sustainability

MDPI

Article

Research on Water Stability and Moisture Damage Mechanism of a Steel Slag Porous Asphalt Mixture

Xiaobing Chen [1,2,*], Miao Zhang [1,*], Jianming Yao [3], Xiaofei Zhang [4], Wei Wen [5], Jinhai Yin [6] and Zhongshan Liang [6]

1 School of Transportation, Southeast University, Nanjing 211189, China
2 Architects and Engineers Co., Ltd., Southeast University, Nanjing 210096, China
3 Suzhou Jiaotou Construction Management Co., Ltd., Suzhou 215007, China; jianmyao@sina.com
4 Kunshan Traffic Development Holdings Group Co., Ltd., Suzhou 215300, China; gongcjsglb5@ktdc.cn
5 Jiangsu Sinoroad Transportation Science and Technology Co., Ltd., Nanjing 211800, China; 220203258@seu.edu.cn
6 Suzhou Sanchuang Pavement Engineering Co., Ltd., Suzhou 215124, China; yinjinhai1985@139.com (J.Y.); liangzhongshan2008@163.com (Z.L.)
* Correspondence: xbchen@seu.edu.cn (X.C.); 220223201@seu.edu.cn (M.Z.)

Abstract: A steel slag porous asphalt (SSPA) mixture, as the surfacing layer of permeable asphalt pavements, not only ensures the pavement surface drainage and noise reduction functions, but also improves the comprehensive utilization of steel slag resources and the inherent protection of the ecological environment. However, compared with ordinary asphalt mixtures, SSPA is more susceptible to water damage, such as scouring and frost swelling caused by external rainwater intrusion, resulting in the deterioration of the pavement performance. Therefore, it is of good practical imperative to study the water stability and moisture damage mechanism of SSPAs. In this study, the water stability of SSPA, that was subjected to a series of time–temperature H_2O-immersion schemes, was investigated using the pull-out and H_2O-immersion Marshall tests, whilst the microscopic mechanism of moisture damage was studied using the scanning electron microscopy (SEM), Fourier infrared spectroscopy (FTIR), and X-ray diffraction (XRD) tests. The corresponding results showed that: (a) with the increase in the H_2O immersion time, the water stability of SSPA first increased and then decreased; and (b) the water stability of SSPA was strong under medium-temperature H_2O-immersion or short-term high-temperature H_2O-immersion. SEM, on the other hand, showed that the transition zone spacing was closely related to the chemical adhesion mechanism between the asphalt and steel slag aggregate. Additionally, the FTIR analysis further showed that the steel slag asphalt mastic spectra had new absorption peaks at 3200~3750 cm^{-1}, inherently indicating the existence of chemical bonding between the asphalt and steel slag, with the XRD results showing that $CaSO_4 \cdot 2H_2O$ had a beneficial effect on the water stability of SSPA.

Keywords: steel slag porous asphalt mixture (SSPA); time–temperature H_2O-immersion; water stability; microscopic mechanism; pull-out test; Marshall test; SEM; FTIR; XRD

Citation: Chen, X.; Zhang, M.; Yao, J.; Zhang, X.; Wen, W.; Yin, J.; Liang, Z. Research on Water Stability and Moisture Damage Mechanism of a Steel Slag Porous Asphalt Mixture. *Sustainability* **2023**, *15*, 14958. https://doi.org/10.3390/su152014958

Academic Editor: Antonio D'Andrea

Received: 1 September 2023
Revised: 4 October 2023
Accepted: 12 October 2023
Published: 17 October 2023

1. Introduction

Under the background of more and more attention to environmental protection, an environmentally friendly asphalt mixture has been widely studied in the field of road engineering [1,2]. However, the production of environmentally friendly asphalt mixtures or other asphalt mixtures for road construction consumes a large amount of natural aggregates, whose quarrying is not only a depletion of natural resources but also an environmental degradation and atmospheric pollution [3–7]. For countries like China, which is one of the world's largest steel makers, a lot of steel slag that is produced as a byproduct of steelmaking also detrimentally contributes to environmental degradation, including land occupation problems, disposal issues, water contamination, etc. [8–10]. To aid in

conserving the limited natural resources, address disposal problems, competing land use issues, and minimize environmental pollution, research into recycling and re-use of steel slag waste has become a hot topic in the past decades [11–14]. Various research studies have found that there is a good adhesion performance between asphalt and steel slag, meaning that steel slag can be potentially substituted for natural aggregates to fabricate steel slag asphalt mixtures [15–17]. Likewise, the literature has also reported excellent anti-cracking properties, good high-temperature performance, durability, etc., for steel slag asphalt mixtures [18–22]. Therefore, steel slag asphalt mixtures constitute a viable candidate for use in road construction [23].

On the other hand, several dense-graded asphalt mixtures that are commonly used in pavements for urban road construction often tend to have poor drainage performance, leading to frequent urban waterlogging problems. However, the use of permeable or porous asphalt mixtures, with superior surface drainage characteristics, has demonstrated to be one of the viable engineering solutions to mitigate this issue [24–26]. Thus, to improve urban flood control and drainage capacity, many cities in China have set off on a wave of constructing sponge cities, with permeable or porous asphalt pavements becoming an integral transportation infrastructure for urban road construction in these sponge cities [27–31].

Likewise, steel slag can be substituted for natural aggregates to prepare steel slag porous asphalt mixtures (SSPAs). However, SSPA has a large gap gradation structure. Therefore, rainwater is more likely to enter its internal structure, with the interface between the asphalt and steel slag potentially suffering moisture damage, resulting in the weakening of the adhesion of the asphalt–steel slag bonding and asphalt itself (i.e., cohesive bonding), ultimately changing the morphological and internal structure of the SSPA matrix [32–36]. Particularly during heavy prolonged rainfall seasons and cold weather, the SSPA mixtures are more susceptible to suffering from moisture damage, including scouring, frost swelling, interfacial debonding, spalling, peeling off, etc., resulting in the decay of pavement performance, durability, and longevity [37]. To aid in mitigating this issue, and optimize the pavement performance, it is thus imperative to study the water stability and moisture damage mechanism of SSPA.

Two methodological approaches are often employed to measure and quantitatively evaluate the water stability of asphalt mixtures. One approach is to assess the water stability of the asphalt mixture indirectly through H_2O immersion tests, pull-out tests, surface energy tests, etc., to quantify the adhesive bonding between the aggregate and the asphalt [35,38–41]. Another approach is to directly measure the overall water spalling resistance of the asphalt mixture through the immersion Marshall tests, freeze-thaw splitting tests, immersion Cantabro loss tests, etc. [5,24,42–44]. Whilst the former approach is largely based on the subjective judgment and interpretation of the experimenter on the test results, the latter is based on a quantitative analysis of the test results and some measured parametric indices [45,46].

To quantitatively and morphologically explain the moisture damage mechanism of the asphalt mixture, the changes in the functional groups and chemical composition of the asphalt mortar before and after H_2O-immersion are typically analyzed using the Fourier transform infrared spectroscopy (FTIR) and X-ray diffraction (XRD) tests [47–49]. On the other hand, the literature has reported that changes in the micro-interface of the asphalt mixture before and after H_2O-immersion can be easily assessed using the scanning electron microscopy (SEM) or atomic force microscopy (AFM) tests [5,50–52]. Additionally, more advanced tests, such as nanoindentation, can be readily used to quantitatively analyze the water stability of the asphalt mixture from the asphalt, interfacial, and aggregate phases within the asphalt mixture itself [53].

Based on the foregoing background, this study employed the time–temperature immersion scheme to macroscopically evaluate the water stability of SSPA using the pull-out and H_2O-immersion Marshall tests. The moisture damage mechanism of SSPA was correspondingly analyzed using the SEM, FTIR, and XRD test methods. Similarly, the interactive

effects of the immersion temperature and immersion time on the water stability of SSPA were also assessed and are discussed in this paper. In the subsequent section, the materials and test methods were discussed, followed by a presentation, analysis, and synthesis of the experimental results. This paper then concluded with a summation of key findings and recommendations.

2. Materials and Test Methods

2.1. Raw Materials

Styrene–butadiene–styrene (SBS) modified asphalt, which was obtained from Suzhou Sanchuang Road Engineering Co., Ltd. (Suzhou, China) in Jiangsu Province, was used in this study. The SBS content was 4.50% by weight. Its technical properties include after the RTFOT, based on the Chinese specification JTG E20-2011 [54], are listed in Table 1.

Table 1. Technical properties of the SBS-modified asphalt.

Test		Unit	Test Result	Spec Requirement [55]
Penetration (25 °C, 100 g, 5 s)		0.1 mm	55.9	40~60
Softening point		°C	82.5	≥60
5 °C ductility		cm	34.6	≥20
Elastic recovery (25 °C)		%	94	≥70
Kinematic viscosity (135 °C)		Pa·s	2.36	≤3
After RTFOT	Mass loss ratio	%	0.14	≤0.6
	Penetration ratio (25 °C)	%	80	≥65
	Ductility (5 °C)	cm	22.6	≥15

Legend: RTFOT = rolling thin-film oven test.

The coarse aggregate used was converter steel slag, which was provided by the Jiangsu Yonggang Group of Companies (Zhangjiagang, China). Its technical indices are shown in Table 2.

Table 2. Technical indices of the steel slag coarse aggregates.

Test	Unit	Test Result	Spec Requirement [56]
Apparent relative density	-	3.549	≥2.90
Water absorption rate	%	1.59	≤3.0
Crushing value	%	13.4	≤26
Los Angeles abrasion loss	%	10.7	≤26
Flat elongated particles content	%	10.1	≤12
Water washing method <0.075 mm particle content	%	0.47	≤1
Adhesive performance	-	5	≥4
Polished stone value (PSV)	-	52	≥42

The fine aggregate used in this study was steel slag, with a particle size of 0~5 mm, which was also supplied by the Jiangsu Yonggang Group Companies (Zhangjiagang, China)—the same source as for the coarse steel slag aggregate. The technical indices are shown in Table 3. Likewise, the technical indices of the limestone powder used are summarized in Table 4.

Table 3. Technical indices of the steel slag fine aggregates.

Test	Unit	Test Result	Spec Requirement [56]
Apparent relative density	-	3.408	≥2.90
Water absorption rate	%	4.75	-
Sand equivalent	%	95	≥60
Water washing method <0.075 mm particle content	s	2.0	≤3
Angularity (flow time)	s	45	≥40

Table 4. Technical indices of the limestone powder.

Test		Test Result	Spec Requirement [57]
Apparent relative density		2.684	≥2.60
Water content/%		0.6	≤1
Particle size range	<0.6 mm	100	100
	<0.15 mm	100	90~100
	<0.075 mm	99.3	75~100
Appearance		Uniform, no agglomerate	No agglomerate
Hydrophilicity coefficient		0.52	≤0.8
Heating stability		No change in color	No change in color

The Tafpack Super (TPS) modifier was sourced from Japan. Its dosage was 8% of the SBS-modified asphalt by weight, and its technical indices are shown in Table 5.

Table 5. Technical indices of the TPS modifier.

Test	Unit	Test Result	Spec Requirement [58]
Appearance	-	Uniform, yellow, granular, and full	Granular, uniform, and full-bodied
Density	g/cm^3	0.58	≤1.0
Melt index	g/10 min	8	≥2.0
Single particle mass	g	0.023	≤0.03

The polyester fibers were sourced from Xutai Company (Taicang, China), and the dosage was 0.3% of the total asphalt mixture by weight. Their technical indices are shown in Table 6.

Table 6. Technical indexes of the polyester fibers.

Test	Unit	Test Result	Spec Requirement [59]
Oil absorption rate	times	5.5	-
Average length	mm	6	4.5~7.5
Average diameter	μm	15.2	15~25
Fracture strength	MPa	527	≥450
Fracture elongation	%	25	≥20
Density	g/cm^3	1.34	-
Melting point	°C	255~265	≥240

2.2. Preparation of the Steel Slag Asphalt Mortar

When the volume ratio of the filler to asphalt (i.e., F/A) is 0.4~0.5, the interaction between the asphalt and aggregate can be fully developed [60]. In this study, the F/A ratio of 0.4 and the density of the material were used to determine the weight ratio of steel slag powder to asphalt, and then to prepare the steel slag asphalt mortar (SSAM). The specific preparation process was as follows: the dried steel slag aggregate was first ground into powder using an electromagnetic sample mill, and thereafter, the steel slag powder of 0.075~0.15 mm sieve size was screened for its use as a filler. Then, the steel slag powder was poured into the 170 °C SBS-modified asphalt based on the F/A ratio of 0.4. The blend was then stirred at a rate of 100 rpm for about 30 min to ensure that the asphalt and steel slag powder were homogeneously mixed. Thereafter, the hot asphalt mortar was poured into the corresponding molds for subsequent sample fabrication. At minimum, three sample replicates were fabricated per test type per material per test variable.

2.3. Preparation of the SSPA Mixture

This study adhered to the Chinese specification CJJ/T 190 [61], with the aggregate gradations blended as shown in Table 7 and Figure 1. In line with typical porous asphalt mixtures, the design air void ratio was 20 ± 2% [24,62,63], with 16% of the gradation passing the 2.36 mm sieve size (Table 7) and an optimal asphalt–aggregate ratio of 5.1% by weight. The mixing time of the SSPA was 3 min at 180 °C, with a 70~80 rpm mixing rate. The molding and compaction temperature was 160 °C. For each material and test condition, three sample replicates were fabricated at 50 blows using the Marshall double-sided compaction method [64].

Table 7. Aggregate gradation for the SSPA mixture.

Gradation	Mass Percentage (%) Passing in Each Sieve Size (mm)									
	16	**13.2**	**9.5**	**4.75**	**2.36**	**1.18**	**0.6**	**0.3**	**0.15**	**0.075**
Design grading	100	98.5	64.7	21.0	16.2	12.4	9.0	7.2	6.1	4.8
Upper limit	100	100	80	30	22	18	15	12	8	6
Lower limit	100	90	50	12	10	6	4	3	3	3
Median	100	95	65	21	16	12	9.5	7.5	5.5	4.5

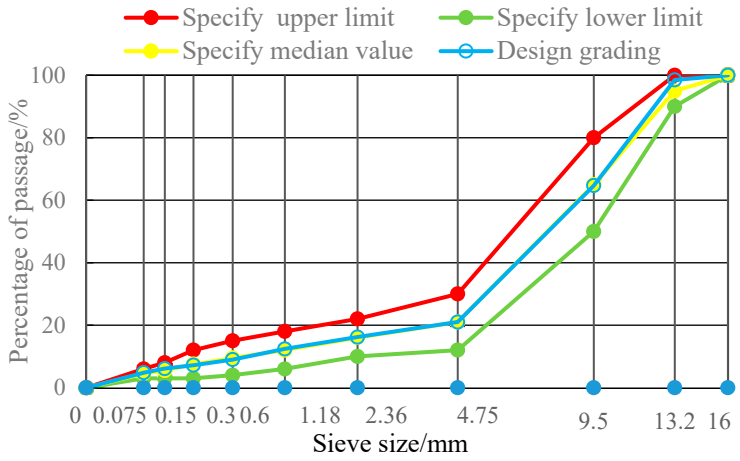

Figure 1. The SSPA gradation curve.

2.4. Test Methods

2.4.1. Time–Temperature H_2O-Immersion Testing

In this study, the time–temperature H_2O-immersion test [65] was used to pretreat the asphalt mixture samples for moisture damage assessment. The degree of moisture damage and performance changes of the SSPA were evaluated after subjecting the SSPA to different H_2O immersion temperatures (namely 20 °C, 40 °C, 60 °C, and 80 °C) and H_2O immersion times (namely 2 d, 4 d, 6 d, and 8 d) to simulate in-service permeable asphalt pavements under different field conditions, with respect to temperature variations and moisture submersion. The 20 °C and 40 °C H_2O immersion temperatures were selected to simulate the Chinese medium-temperature conditions, whilst the 60 °C and 80 °C H_2O immersion temperatures were used to simulate the high-temperature environmental conditions [66].

2.4.2. Pull-Out Testing

The pull-out test is the process of testing the structural layer under the action of a constant vertical pull-out force until the maximum pull-out tensile force is generated, which is known to measure the bonding performance of the interlayer, such as road base-subbase layers or granular material layers [67,68]. In this paper, the pull-out test was used to study the adhesion of steel slag and asphalt after time–temperature H_2O-immersion, and to

evaluate the water stability of SSPA, and is photographically shown in Figure 2 [40]. The first step was to cut the large steel slag aggregates into small blocks using a SYD-0850 asphalt mixture plate cutting machine. Thereafter, cement mortar was prepared to affix the steel slag cubes to the test molds. The test mold, containing the steel slag cubes and cement mortar, was then put into a wet-air protection box for 24 h, curing at ambient temperature, followed by the removal of the molds. Thereafter, liquefied asphalt was evenly coated onto the aggregate surfaces, following the time–temperature H_2O-immersion curing sequence that was described in Section 2.4.1 of this paper.

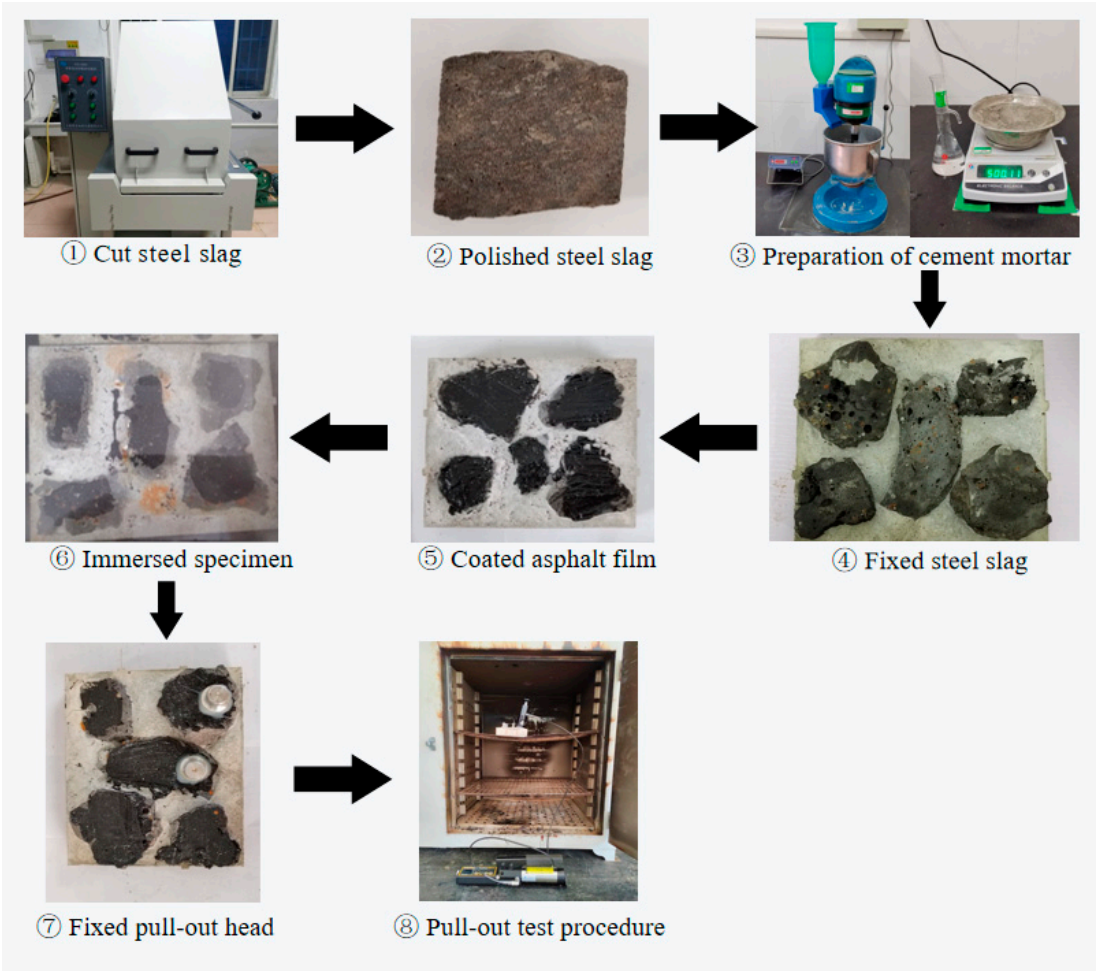

Figure 2. The pull-out test.

After sample curing, a 20 mm diameter pull-out head was slowly pressed vertically onto the surface of the asphalt film with WD1001 high-performance structural glue. Thereafter, the pull-out head was affixed onto the asphalt film and left to cure/harden for 24 h at ambient temperature. Lastly, a PosiTest At-M manual adhesion tester was used for conducting the pull-out test in a 20 °C constant temperature oven. The maximum pull-out tensile force to sample failure (i.e., fracture separation) was accordingly recorded during this test. The pull-out test was repeated three times for each sample group, with the average of the three replicates taken as the final test result.

2.4.3. H_2O-Immersion Immersion Marshall Testing

In this study, the SSPA cylindrical samples (101.6 mm ± 0.25 mm diameter by 63.5 mm ± 1.3 mm in height) were compacted using an electric Marshall compaction machine (i.e., 50 times on each sample side), in accordance with the T 0709 test method of the Chinese specification JTG E20-2011 [54]. Thereafter, the samples were randomly divided

into 20 different groups and accordingly numbered, namely the control and experimental groups. The samples, both control and experimental groups, were then subjected to a series of temperature (20 °C, 40 °C, 60 °C, and 80 °C) and time (0.5 h, 2 d, 4 d, 6 d, and 8 d) H_2O-immersion tests, with no less than four samples in each group. Thereafter, the time–temperature H_2O-immersion Marshall test was performed on the SSPA samples.

2.4.4. Scanning Electron Microscopy (SEM) Testing

For SEM testing [50,69], the SSPA samples were first cut and polished into 1 cm^3 cubic specimens. After time–temperature H_2O-immersion curing, as previously described in Section 2.4.1, they (the 1 cm^3 cubic specimens) were then sprayed with gold using a Q150TS high-resolution sputter coater. Thereafter, the specimens were morphologically and microstructurally observed using a FEI Inspect F50 scanning electron microscope. Three surface positions for each test sample were scanned at different magnifications of ×200, ×500 and ×1000, from which one best representative surface position of each sample was selected for morphological and microstructure analysis.

2.4.5. Fourier Transform Infrared (FTIR) Spectroscopy Testing

In this study, the FTIR testing [47,70] of the steel slag powder, SBS-modified asphalt, and the steel slag asphalt mortar, after a series of time–temperature H_2O-immersion sequences (see Section 2.4.1), was carried out using a Nicolet IS10 Fourier transform infrared spectrometer sourced from Thermo Company, Waltham, MA, USA. The test wave number range was 400~4000 cm^{-1}, with a resolution of 2 cm^{-1}. The captured test data were processed and analyzed by converting the time domain function interferometric images into ordinary infrared spectrograms using a Fourier transformation [71] and the OMINIC8.0 software [72]. The FTIR test was repeated three times for each sample, with the corresponding average serving as the final test result.

2.4.6. X-ray Diffraction (XRD) Testing

For XRD testing [73], a D8-Discover X-ray diffractometer from Bruker (Hamburg, Germany) was used to analyze the chemical phases of the steel slag powder and steel slag asphalt mortar after a series of time–temperature H_2O-immersion sequences, which have been described in Section 2.4.1 of this paper. A step scan, with an angle range from 5° to 80° and a scan rate of 2°/min, was used. The XRD test data were processed and analyzed using the Jade9.0 software [74]. For each sample, the XRD test was repeated three times, with the corresponding average serving as the final test result.

3. Experimental Test Results and Analysis

3.1. Macro Test

In this study, the effects of H_2O immersion temperature and time on the water stability of SSPA was evaluated from a macro multiscale perspective. The pull-out test was used for indirectly evaluating the water stability of SSPA by analyzing the adhesion properties between the asphalt and steel slag aggregates, while the H_2O-immersion Marshall test was used for the direct evaluation of the water stability of SSPA. The results of these tests have been analyzed and synthesized below.

3.1.1. Analysis of the Results of the Pull-Out Test

(1) Damage Evaluation Indicators

The pull-out test causes adhesion, cohesive, mixed, and dislodgement damage. These damage mechanisms, along with their corresponding results, have been discussed in the subsequent text [75].

1. As shown in Figure 3a, adhesion damage refers to the damage of the adhesive interface between the asphalt and aggregate [69]. When this occurs, there is either almost no residual asphalt film or only a small amount of asphalt film on the aggregate surface.

However, there is typically no significant damage within the aggregate or within the asphalt.

2. As shown in Figure 3b, cohesive damage refers to the internal damage within the asphalt itself [69], without the adhesion damage between the asphalt and aggregate.
3. As shown in Figure 3c, mixed damage refers to the damage of the adhesive interface between the asphalt and aggregate, accompanied by internal damage within the asphalt [69]. With this damage mechanism, some asphalt film remains on the aggregate surface, but cannot be completely determined as adhesion or cohesive damage.
4. As shown in Figure 3d, dislodgement damage refers to the form of damage that occurs between the asphalt and the pull-out head [69]; that is, there is dislodgement of the asphalt from the pull-out head. Under this condition, the surface of the asphalt film on the surface of the aggregate is flat, with all the asphalt film remaining on the surface of the aggregates. On the surface of the pull-out head, there would be none or only a very small amount of the asphalt film remaining.

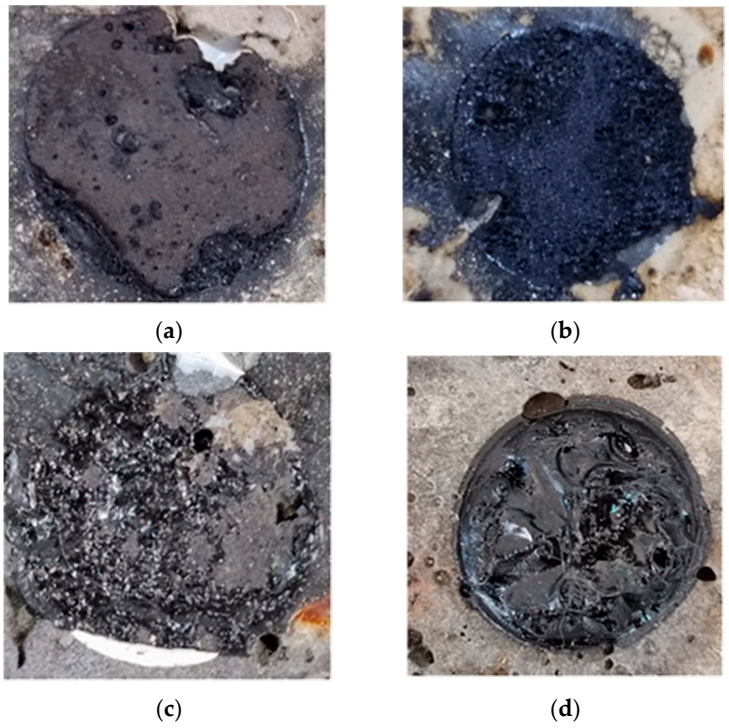

Figure 3. Pull-out test damage mechanisms. (**a**) Adhesion damage. (**b**) Cohesive damage. (**c**) Mixed damage. (**d**) Dislodgement damage.

(2) Test Results

The damage results from the pull-out test for the asphalt and steel slag after a series of time–temperature H_2O-immersion sequences are shown in Table 8.

Table 8. Damage pull-out test results after time–temperature H_2O-immersion sequences.

Immersion Time/d	Damage Mechanism at Different Temperatures			
	20 °C	**40 °C**	**60 °C**	**80 °C**
0	Dislodgement	Dislodgement	Dislodgement	Dislodgement
2	Cohesive	Cohesive	Cohesive	Cohesive
4	Cohesive	Cohesive	Cohesive	Cohesive
6	Cohesive	Cohesive	Mixed	Adhesion
8	Cohesive	Mixed	Adhesion	Adhesion

As can be seen from Table 8, under dry different temperature conditions without H_2O immersion, the prevalent damage mechanism is dislodgement, indicating that the adhesion strength between the asphalt and steel slag aggregates prior to time–temperature immersion was greater than the adhesion strength between the asphalt and the pull-out head; meanwhile, the adhesive force within the asphalt itself prior to time–temperature immersion was also greater than the adhesion strength between the asphalt and the pull-out head. After 2~8 d–20 °C H_2O immersion and 2~6 d–40 °C H_2O immersion, pull-out damage mainly occurred in the interior of the asphalt, resulting in cohesive damage, with the degree of damage strength depending on the asphalt's cohesive strength. After 8 d–40 °C H_2O immersion, mixed damage occurred, indicating that after a long time of medium-temperature H_2O-immersion action, the adhesion within the asphalt itself gradually decreased. During this stage, as the surface energy of the water molecules was lower than that of asphalt, and the polarity of the water molecules was also higher than that of asphalt, it can separate or replace the asphalt on the steel slag surface partially [76]; at medium temperature, the water molecules continued to erode the interface between the asphalt and steel slag aggregates for eight days; ultimately, cohesive damage transformed into mixed damage. At high-temperature conditions, and with the H_2O immersion time having been increased, the pull-out damage evolved rapidly from cohesive to mixed failure. Thereafter, adhesion damage occurred, indicating that the asphalt adhesion under high-temperature H_2O-immersion conditions significantly reduced; that is, the increase in temperature and time resulted in the following effects: (a) made the asphalt softer to flow, and (b) increased the diffusion speed and destructive power of the high-temperature water molecules at the interface between the asphalt and steel slag. Water molecules are more likely to remove the asphalt from the steel slag surface, which correspondingly reduced the adhesion bonding between the asphalt and steel slag. Under these conditions, the asphalt film was easily peeled off from the surface of the steel slag aggregates during the pull-out test.

Based on the pull-out damage mechanism, the pull-out strength was categorized into adhesion strength, cohesive strength, mixed strength, and dislodgement damage strength. The results of the pull-out strength after time–temperature H_2O-immersion are shown in Figure 4.

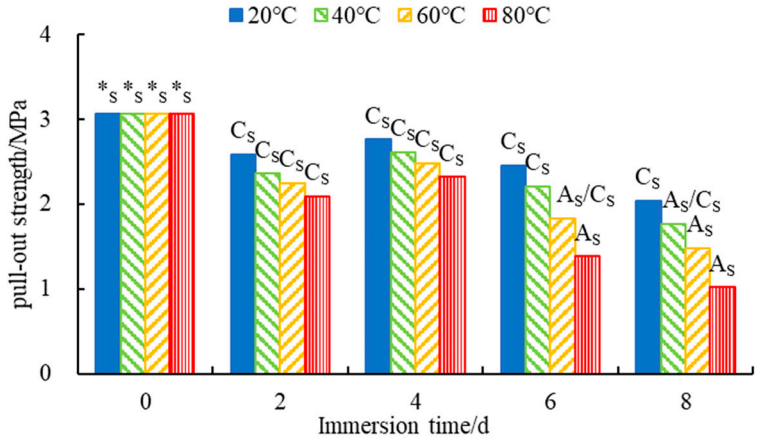

Figure 4. Pull-out strength results after time–temperature H_2O-immersion. *s indicates the dislodgement damage strength; A_S indicates the adhesion damage strength; C_S indicates the cohesive damage strength; and A_S/C_S indicates the mixed damage strength.

As can be seen from Figure 4, the pull-out strength at different H_2O immersion temperatures for 0 days were quantitatively the largest, with all of them associated with dislodgement damage. With an increase in the H_2O immersion time (except 0 days of H_2O immersion), the pull-out strength, at different temperatures, firstly indicated an increasing trend and thereafter decreased. With an increase in the H_2O immersion temperature, the

pull-out strengths showed different degrees of decay. After 2~4 days of H_2O immersion at different temperatures, the pull-out strength was predominantly cohesive strength, mostly depending on the cohesive strength of the asphalt. Under these conditions, the water molecules mainly eroded the asphalt film. This was exacerbated by the fact that the increase in temperature makes the asphalt softer and reduces the asphalt viscosity, resulting in a decay in the asphalt's cohesive strength. Likewise, the asphalt film on the surface of the steel slag aggregates will also begin to flow, inherently allowing the water molecules from the side of the asphalt film to diffuse into the interface between the asphalt and steel slag aggregate.

Compared with 2 days of H_2O immersion, the samples at 20 °C, 40 °C, 60 °C, and 80 °C had an increase in the pull-out strength of about 7%, 10.7%, 10.4%, and 11.0%, respectively. After 4 days of H_2O immersion, the overall adhesion performance between the asphalt and steel slag aggregates improved. This was partly because the chemical reaction between the more alkaline compounds contained in the steel slag aggregates and the acidic asphalt formed a stronger chemical bond during the H_2O-immersion process. With an increase in the H_2O immersion temperature, the chemical reaction between the asphalt and steel slag aggregates was also accelerated, and further contributed to enhancing the interfacial bonding strength.

After medium-temperature (i.e., 6~8 d at 20 or 40 °C) H_2O-immersion, the pull-out strength was mostly related to cohesive damage. With an increase in the immersion time and temperature, the pull-out strength gradually decreased, evolving from cohesive to mixed damage strength. After high-temperature (i.e., 6~8 d at 60 or 80 °C) H_2O immersion, the pull-out strength gradually evolved from cohesive to mixed damage strength; that is, the damage mechanism changed from cohesive to mixed damage. With respect to adhesive damage, the associated pull-out strength (adhesion) between the asphalt and steel slag aggregates was relatively smaller and significantly decreased with an increase in the H_2O immersion time and temperature. After long-term H_2O immersion, the water molecules tended to erode into the interface between the asphalt and steel slag aggregate. This is partly because the adhesion properties between the water molecules and steel slag aggregates are greater than that between the asphalt and steel slag aggregates [15,77,78], with the water film replacing the asphalt film on the surface of the steel slag aggregates, inherently leading to the asphalt film on the surface of the steel slag aggregate to be easily pulled off during the pull-out test. Compared with medium-temperature H_2O immersion, the high-temperature water molecules at the asphalt and steel slag aggregate interface diffused rapidly due to the high temperature effects and correspondingly enhanced the emulsification of the asphalt. The long-term effects of this high-temperature H_2O-immersion sequence is poor volume stability of the steel slag aggregates with potential for swelling [79], further reducing the stability of the asphalt and steel slag aggregate interface, including the adhesion strength.

3.1.2. Analysis of the Results of the H_2O-Immersion Marshall Test

As can be seen from Figure 5, at 20 °C, 40 °C, 60 °C, and 80 °C temperature conditioning after 2 days of H_2O immersion, the residual stability of the SSPA samples were 103%, 100%, 94%, and 88%, respectively. All these numbers are greater than 85% and satisfactorily meet the Chinese specification JTG/T 3350-03 [57] of a minimum residual stability requirement of 85%. Therefore, the SSPA's high-temperature water stability after 2 days of H_2O immersion was deemed to be satisfactory.

However, after 6 d–80 °C H_2O immersion, the residual stability of the SSPA dropped to 81%, i.e., about four percentage points below the Chinese specification JTG/T 3350-03 [57] requirement of 85%. This indicated that the water stability of the SSPA reduced after a long duration (>4 days) of high-temperature H_2O immersion at 80 °C; that is, the moisture damage under high-temperature H_2O immersion was more severe than that under medium-temperature H_2O immersion.

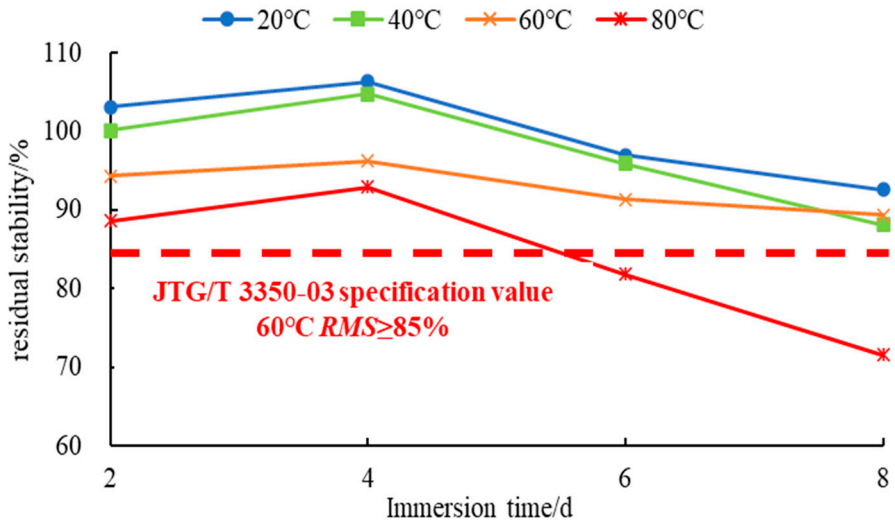

Figure 5. Effect of time–temperature immersion on the residual stability of SSPA.

From two to four days, the residual stability first increased and thereafter decreased, with an increase in the H_2O immersion time at different H_2O immersion temperatures. However, the residual stability significantly decreased with an increase in temperature. As the surface of the steel slag aggregates is rough and alkaline, it tends to have a better adhesion with the weakly acidic asphalt [80]. In the early stages of H_2O immersion, an acid–base chemical reaction occurred between the steel slag aggregates and asphalt; the alkanes in asphalt are easy to react with the silicon-containing compound on the surface of the steel slag to generate the silane [15,81], which inherently provided the chemical adhesive force and correspondingly improved the water stability of the SSPA. Furthermore, the asphalt film on the steel slag aggregate surfaces played a crucial role in enhancing the water resistance and reducing the possibility of hydration of the steel slag aggregates, as well as inhibiting the volume expansion of the steel slag aggregates. However, with an increase in the H_2O immersion time and temperature, the adhesion between the asphalt and steel slag aggregates decreased; this led to the asphalt film on the surfaces of the steel slag aggregates to gradually fall off, with the pores on the surfaces of the steel slag aggregates quickly absorbing a lot of water [82]; that is, the volume stability of the steel slag aggregates declines and contributes to weakening the internal stability of the structure of SSPA, causing surface volume expansion of the SSPA and, ultimately, a decrease in the water stability.

3.2. Microscopic Test

At a macroscopic level, the pull-out test results indicated that after 2~6 d–60 °C H_2O immersion, the damage mechanism rapidly evolved from cohesive to mixed damage, while adhesion damage appeared after a long time (>4 days) of high-temperature H_2O immersion. On the other hand, the H_2O-immersion Marshall test results indicated that after 2~6 d–60 °C or 80 °C H_2O immersion, the residual stability of SSPA first increased and then decreased. At 6 d–80 °C H_2O immersion, the residual stability of SSPA was 81%, which does not meet the 85% Chinese JTG/T 3350-03 [57] specification requirements. In addition, after medium-temperature H_2O immersion, the results of the pull-out test were mostly cohesive damage, and the residual stability of SSPA was greater than 85%, which met the Chinese JTG/T 3350-03 specification requirements. Therefore, we selected the most representative experimental data, and analyzed the reason for why the water stability of SSPA first increased and then decreased through 2~6 d–60 °C H_2O immersion, and comparatively analyzed the reason for why the residual stability of SSPA was lower than 85% through 6 d–60 °C or 80 °C H_2O immersion. To sum up, based on the macroscopic test data, SEM, FTIR, and XRD tests on SSPA and SSAM samples after 2~6 d–60 °C and

6 d–80 °C H_2O immersion were conducted to microscopically analyze the moisture damage mechanism of SSPA after time–temperature H_2O-immersion curing.

3.2.1. Changes in the SSPA's Micro-Interface after Time–Temperature H_2O-Immersion

Figures 6–9 show the SEM results of the asphalt–steel slag aggregate interface in the SSPA after medium- and high-temperature H_2O immersion. In the figure, ① referred to the adhesion area of asphalt film on the surface of steel slag aggregates; ② referred to the compound phase area of asphalt and steel slag formed by physical and chemical interaction between asphalt and steel slag aggregates. As shown in Figure 6, the asphalt film thickness was uniform and tightly wrapped on the surface of the steel slag aggregates after the 2 d–60 °C H_2O-immersion curing. The interface transitional zone of the asphalt–steel slag aggregates was also uniform and flat. After 4 d–60 °C H_2O immersion, Figure 7 shows a substance with a white color (i.e., possibly $CaCO_3$, C-S-H, and $CaSO_4 \cdot 2H_2O$, etc.) produced via the chemical reaction between the asphalt and hydration product of steel slag. Additionally, it was also observed that the white substance was uniformly distributed in the transitional zone of the asphalt–steel slag interface, which ultimately filled up the gap of the interfacial transition zone (ITZ) and provided a good mechanical bond. This indicates the asphalt film closely adhered to the surface of the steel slag aggregate and can adsorb more free asphalt to form structural asphalt, leading the ITZ to be denser and flatter, ultimately improving the water stability of SSPA. Furthermore, in Figure 7c, compared with Figure 6c, it can be found that there were many more pores on the asphalt surface, which was due to the water molecules gradually eroding the asphalt with an increase in the H_2O immersion time, and the surface of the steel slag was even denser, indicating that under these H_2O immersion conditions the asphalt itself is damaged by water molecules, and the products of the chemical reaction between the steel slag and the asphalt adhered to the steel slag surface, protecting the steel slag from the water molecules.

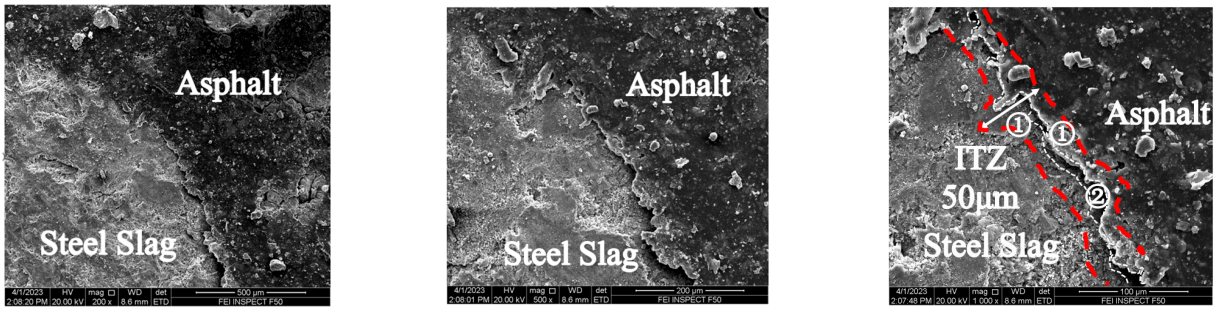

(**a**) (**b**) (**c**)

Figure 6. Microscopic morphology of SSPA after 2 d–60 °C H_2O immersion: (**a**) ×200 magnification; (**b**) ×500 magnification; and (**c**) ×1000 magnification.

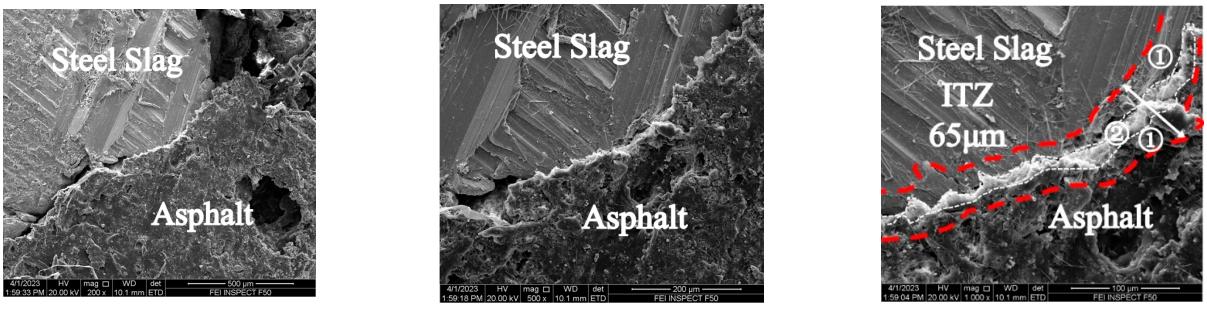

(**a**) (**b**) (**c**)

Figure 7. Microscopic morphology of SSPA after 4 d–60 °C H_2O immersion: (**a**) ×200 magnification; (**b**) ×500 magnification; and (**c**) ×1000 magnification.

(**a**) (**b**) (**c**)

Figure 8. Microscopic morphology of SSPA after 6 d–60 °C H_2O immersion: (**a**) ×200 magnification; (**b**) ×500 magnification; and (**c**) ×1000 magnification.

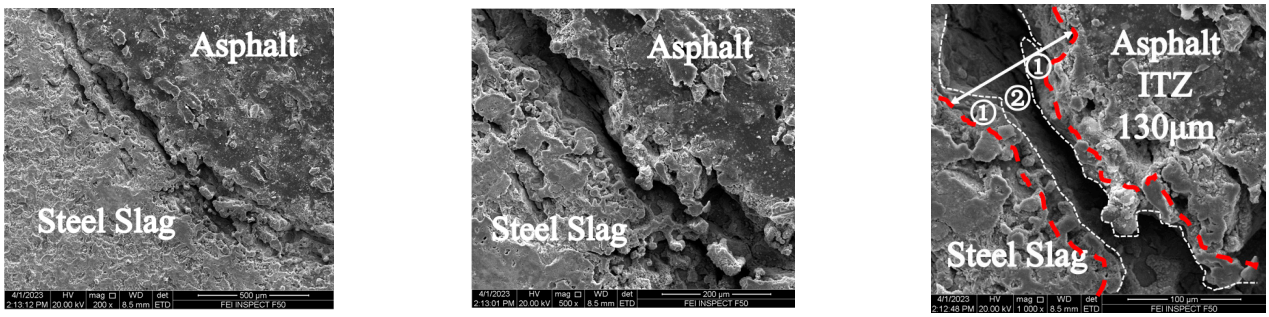

(**a**) (**b**) (**c**)

Figure 9. Microscopic morphology of SSPA after 6 d–80 °C H_2O immersion: (**a**) ×200 magnification; (**b**) ×500 magnification; and (**c**) ×1000 magnification.

As shown in Figure 8, a substance with a white color in the ITZ disappeared after 6 d–60 °C H_2O immersion, possibly because the high-temperature and longer H_2O immersion time made calcium carbonate, hydrated calcium silicate, and calcium sulfate dihydrate to decompose and flake off. The water film in the micro gap replaced the asphalt film wrapped on the surface of the steel slag aggregates, with the asphalt film thickness decreasing and gradually flaking off from the surface of the steel slag aggregates, ultimately reducing the adhesion bond between the asphalt and steel slag aggregates. Furthermore, pores appeared on the surface of the steel slag, indicating that water molecules are beginning to erode the steel slag.

In Figure 9, the asphalt film on the surface of the steel slag aggregates peeled off after 6 d–80 °C H_2O immersion, indicating that the surface area between the steel slag aggregates and asphalt film becomes smaller; the ITZ also increased, while the adhesion force decreased [83,84]. Under these conditions, the high-temperature water molecules diffused within the interface between the asphalt and steel slag aggregates at a relatively high speed with considerable destructive force. In addition, asphalt is a viscoelastic and temperature-sensitive material [85–87]. Therefore, the 80 °C high temperature would inherently reduce the viscosity and enhance the fluidity of the asphalt, ultimately leading to a decay in the water stability of SSPA. Figure 10 shows a plot of the ITZ as a function of H_2O immersion temperature and time.

As shown in Figure 10, the width of the ITZ between the asphalt and steel slag kept on increasing with an increase in the H_2O immersion temperature and time. Under this condition, the adhesion between the asphalt and steel slag aggregates decreased, and moisture damage phenomena, such as cracking, bulging, peeling off, and aggregate loss, appeared. To mitigate this and improve the water stability of SSPA, an appropriate amount of anti-stripping agent, such as desulphurization ash, can be added to the SSPA to improve the adhesion between the asphalt and steel slag aggregates [88].

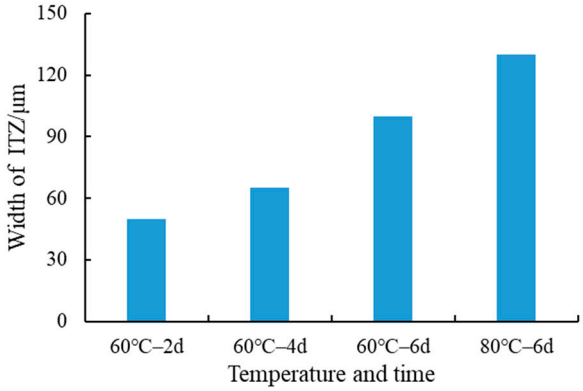

Figure 10. Width of the ITZ of SSPA after H_2O immersion.

3.2.2. Changes in the SSAM's Functional Groups after Time–Temperature H_2O-Immersion

From Figures 10 and 11, it is seen that in the functional group region of the infrared spectrum 1330 cm^{-1}~4000 cm^{-1}, the absorption peaks of each group of steel slag asphalt mortar appear around the wave numbers of 3554 cm^{-1}, 2923 cm^{-1}, 2852 cm^{-1}, 1600 cm^{-1}, 1523 cm^{-1}, 1460 cm^{-1}, and 1380 cm^{-1}. These absorption peaks were generated via the stretching vibration of the chemical bonds. The infrared spectrum fingerprint region of 400 cm^{-1}~1300 cm^{-1} not only contains simple stretching vibrations of the single bonds, but also includes the characteristic spectrum generated via the deformation vibration, reflecting the subtle changes in the molecular structure [15]. In Figure 11, there are 966 cm^{-1}, 862 cm^{-1}, and 513 cm^{-1} characteristic peaks in the fingerprint area of the infrared spectrum, namely: (a) the 966 cm^{-1} peak is the out-plane bending vibration of the trans-CH molecules in the asphalt, (b) the 862 cm^{-1} peak is the out-plane bending vibration of the CH molecules in the benzene ring, and (c) the 513 cm^{-1} absorption peak is more consistent with the inorganic compound group profile of CaO, Al_2O_3, and Fe_2O_3 of β-dicalcium silicate, or tricalcium silicate contained in steel slag [89].

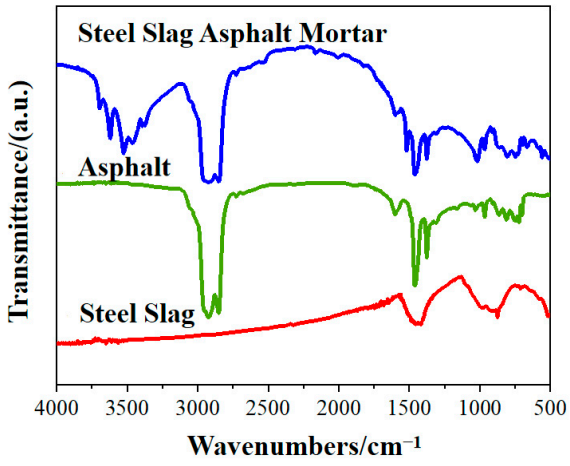

Figure 11. Infrared spectra of the asphalt, steel slag, and steel slag asphalt mastic.

In Figure 12, the absorption bands near the absorption peaks at 3554 cm^{-1} and 1523 cm^{-1} are unique to the steel slag asphalt mortar, whilst the absorption peaks at 3554 cm^{-1} are generated via the stretching vibrations of amine and amide N-H and SiO-H. The absorption peak at 1523 cm^{-1}, on the other hand, may have been caused by the stretching vibrations of the aromatic nitro-NO_2, which could be attributed to the chemical bond between the asphalt and steel slag aggregates. In addition, 2923 cm^{-1} represents the antisymmetric stretching vibration of the C-H molecules in the alkanes and cycloalkanes, 2852 cm^{-1} is the symmetric stretching vibration of the C-H molecules in

the alkanes and cycloalkanes, 1600 cm^{-1} is the backbone stretching vibration of the C=C molecules in the asymmetrically substituted aromatic rings, 1460 cm^{-1} is the antisymmetric angle change vibration of the CH_3 molecules in the alkanes, and 1380 cm^{-1} is the symmetric angle change vibration of CH_3 molecules in the alkanes [90].

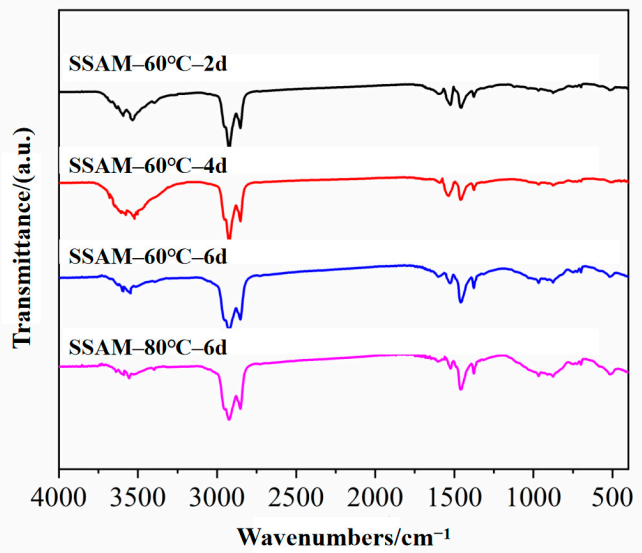

Figure 12. Infrared spectra of the SSAM after H_2O immersion.

In Figure 12, the peak heights and peak areas of the infrared spectra of the steel slag asphalt mortar (SSAM) also changed with the change in the H_2O immersion time and temperature. The peak area ratios of N-H and SiO-H (3554 cm^{-1}), as well as -NO_2 (1523 cm^{-1}), which are unique to the SSAM and reflect the chemical interaction between the asphalt and slag aggregate, were selected as quantitative indicators to quantify the effects of the time–temperature H_2O-immersion scheme on the microstructural composition of the SSAM. The peak area ratios of these characteristic peak functional groups were defined as follows [91,92]:

$$I_{\mathrm{N-H,\ SiO-H}} = A_{3554} / \sum A \quad (1)$$

$$I_{-\mathrm{NO_2}} = A_{1523} / \sum A \quad (2)$$

$$\sum A = A_{3554} + A_{2923} + A_{2852} + A_{1602} + A_{1523} \quad (3)$$

where $I_{\mathrm{N\text{-}H,\ SiO\text{-}H}}$ = amine and amide N-H and SiO-H functional group indices, $I_{\mathrm{\text{-}NO2}}$ = -NO_2 functional group index, A_i = the peak area when the number of waves is i, and $\sum A$ = total peak area.

Figure 13 shows these functional groups as a function of H_2O immersion time. From Figure 13a, it is graphically evident that the difference between the N-H and SiO-H functional group index of the SSAM at 2 d–60 °C versus 4 d–60 °C H_2O immersion is not significant but decreases significantly at 6 days of H_2O immersion. This indicates that the chemical bonding formed via the chemical reaction of the SSAM at the early stage of H_2O immersion was firmly maintained, with the chemical bonding beginning to decay at 6 days of H_2O immersion. In Figure 13b, the -NO_2 functional group index of the SSAM increases and then decreases with an increase in the H_2O immersion time at 60 °C; this trend is similar to the results of the macroscopic tests. The -NO_2 functional group index was the highest at 4 days of H_2O immersion. This infers that the chemical reaction in the SSAM reached its best or optimum state at 4 days of H_2O immersion, which was largely consistent with the results of the macroscopic pull-out and H_2O-immersion Marshall tests. This is partly because the chemical bonding between the asphalt and steel slag aggregates is much stronger than the intermolecular forces [93,94]. This ultimately enhances the adhesion

between the asphalt and steel slag aggregates, forming a thicker structural asphalt that is beneficial to the improvement of the high-temperature stability and water stability of both the SSAM and SSPA. In Figure 14, the functional group indices are plotted as a function of H_2O immersion temperature.

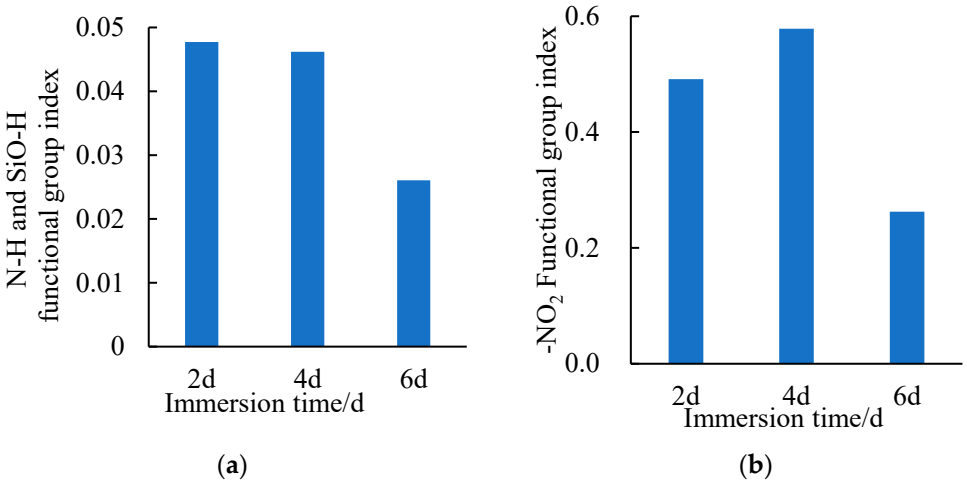

Figure 13. SSAM functional group indices for various H_2O immersion times at 60 °C: (**a**) N-H and SiO-H functional group index; and (**b**) -NO_2 functional group index.

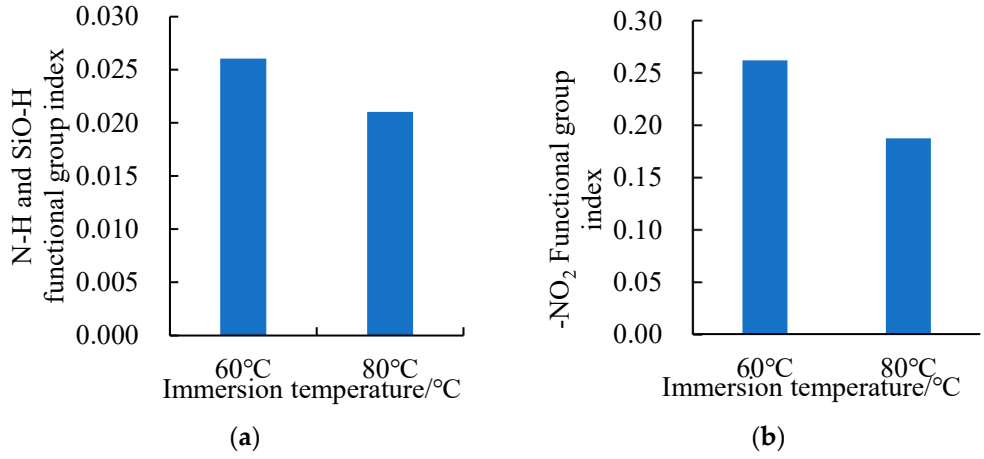

Figure 14. SSAM functional group indices at 6 days of H_2O immersion at various temperatures: (**a**) N-H and SiO-H functional group index; (**b**) −NO_2 functional group index.

As shown in Figure 14, the N-H and SiO-H functional group index and -NO_2 functional group index at 6 days of H_2O immersion decreased significantly with an increase in the H_2O immersion temperature. This suggests that the high-temperature H_2O-immersion scheme had a significant adverse effect on the chemical bonding between the asphalt and steel slag, which severely weakened the interfacial chemisorption of the asphalt and steel slag.

3.2.3. Changes in the SSAM's Chemical Fraction after Time–Temperature H_2O-Immersion

As can be seen in Figure 15, the XRD diffraction pattern of pure steel slag powder exhibits strong diffraction peaks in the range of 2θ = 31°~34°, with crystalline peaks appearing at diffraction angles of about 32.6°, 33.2°, and 33.7°. This corresponds to the crystalline surfaces of $Ca_3(SiO_4)O$, Ca_2SiO_4, and $Ca_3Al_2(SiO_4)_3$, respectively, indicating a high content of calcium silicates and calcium aluminosilicates in the steel slag [95]. Additionally, the crystalline peaks corresponding to FeO appear at diffraction angles of about 61.1° and 73.4°, etc., indicating that the steel slag samples contained more FeO.

In contrast, free calcium oxide (f-CaO) had a weaker diffraction peak intensity in the XRD pattern of steel slag powder, which is partially because f-CaO is decomposed and transformed during the natural aging process of steel slag and when grinding it (steel slag) into powder. In summary, the XRD results showed that the samples contained the main phases of Ca_2SiO_4, $Ca_3(SiO_4)O$, FeO, $CaMg(CO_3)_2$, $Ca_3Al_2(SiO_4)_3$, Mn_3O_4, and CaO. The Mathematics tool under analysis in the menu bar of Origin [96] was used to integrate all the peaks in the XRD patterns of the steel slag powder. The areas of the individual peaks and the total area of all the peaks were calculated. Thereafter, the areas of the peaks corresponding to each phase were divided by the total area of all the peaks to obtain the relative contents of each phase in steel slag powder as 37.3%, 20.2%, 14.2%, 10.2%, 8.2%, 6.5%, and 2.3%.

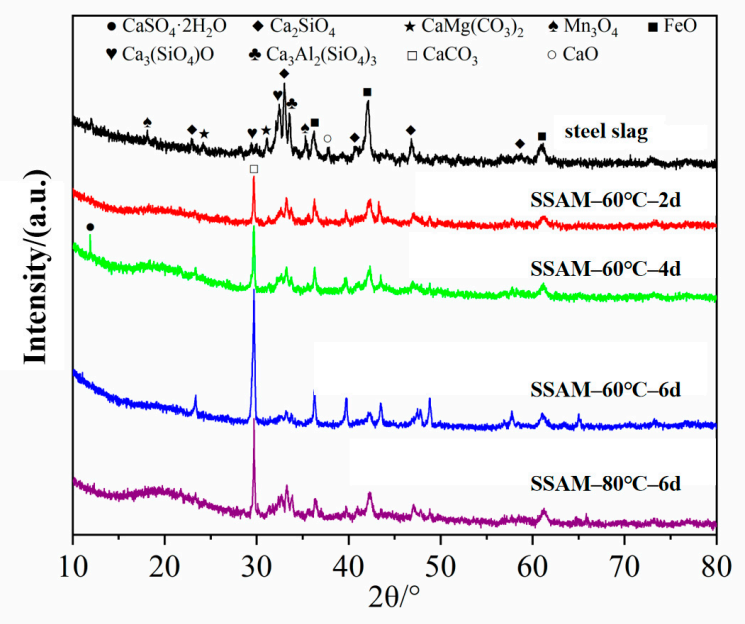

Figure 15. XRD analysis results of steel slag powder and steel slag asphalt mastic.

As visually observed in Figure 15, the XRD peaks of the steel slag powder and all the steel slag asphalt mastic showed little change in the locations of the peaks after the slag powder was mixed with asphalt as a filler. However, the intensity of the peaks decreased, as the asphalt molecules wrapped on the surface of the steel slag powder reduced its diffraction intensity. In contrast, the crystallization peak of $CaCO_3$ at 2 θ = 29.7° showed a significant enhancement and increased with an increase in the H_2O immersion time. With an increase in the H_2O immersion temperature, however, the crystallization peaks mainly decreased due to the hydration reaction of the active components in the steel slag, similar to cement during the H_2O-immersion process, as illustrated below in Equations (4)–(9) [97–99].

$$CaO + H_2O = Ca(OH)_2 \quad (4)$$

$$2CaO \cdot SiO_2 + nH_2O = xCaO \cdot SiO_2 \cdot (n - 2 + x)H_2O + (2 - x)Ca(OH)_2 \quad (5)$$

$$3CaO \cdot SiO_2 + nH_2O = xCaO \cdot SiO_2 \cdot (n - 3 + x)H_2O + (3 - x)Ca(OH)_2 \quad (6)$$

$$Ca(OH)_2 + CO_2 = CaCO_3 + H_2O \quad (7)$$

$$CaCO_3 + H_2SO_4 = CaSO_4 + H_2O + CO_2 \uparrow \quad (8)$$

$$CaSO_4 + 2H_2O = CaSO_4 \cdot 2H_2O \quad (9)$$

In general, the hydration cementation products improved the ITZ, making the asphalt and steel slag structure to be denser, which macroscopically showed an improvement in moisture damage resistance performance. However, the high-temperature H_2O-immersion

environment has a detrimental effect on the hydration cementation products. Compared with the steel slag powder, the crystalline peaks corresponding to FeO, that appeared at diffraction angles of about 61.1° and 73.4°, etc., in the steel slag asphalt mastic were less intense and decreased with an increase in the H_2O immersion temperature and time, indicating that the steel slag asphalt mastic contained less iron compounds.

At 4 d–60 °C H_2O immersion, the XRD patterns of the steel slag asphalt mastic appeared at 2 θ = 11.8° with a characteristic $CaSO_4 \cdot 2H_2O$ crystalline peak. This was largely due to the further acid–base chemical reaction between the various acidic groups contained in the asphalt itself and the $CaCO_3$ produced via the hydration reaction of the steel slag, as shown in Equations (8)–(9) [99,100]. $CaSO_4 \cdot 2H_2O$ is the main component of raw gypsum [100] that enhances the interfacial bonding strength between the asphalt and steel slag aggregates, making it difficult for water to penetrate the interfacial zone. This also substantiates the results that the pull-out strength and residual stability of the SSPA reached its highest values at 4 d–60 °C H_2O immersion in the macro test (refer to Section 3.1 of this paper) and indicates that the white substance observed at the interface between the steel slag and asphalt in the SEM test was $CaSO_4 \cdot 2H_2O$ (refer to Section 3.2.1 of this paper). The analysis of the SSAM-60 °C–6 d and SSAM-80 °C–6 d curves in Figure 15 show that the $CaSO_4 \cdot 2H_2O$ diffraction peaks disappeared with a further increase in the H_2O immersion time and temperature. Under these H_2O-immersion conditions, both the pull-out strength and the residual stability were greatly reduced, indicating that the $CaSO_4 \cdot 2H_2O$ was closely related to the water stability of SSPA. This suggests that the high temperature and long H_2O immersion time caused the decomposition and exfoliation of the calcium sulfate dihydrate that inherently reduced the adhesion performance between the asphalt and steel slag aggregates.

4. Conclusions

In this study, the water stability of SSPA, that was subjected to a series of time–temperature H_2O-immersion sequences, was investigated using the pull-out and H_2O-immersion Marshall tests, while the microscopic mechanism of moisture damage was studied using the SEM, FTIR, and XRD tests. The main findings and conclusions are as follows:

- Both the macroscopic and microscopic tests showed that at a constant H_2O immersion temperature, the water stability of SSPA first increased and then decreased with an increase in the H_2O immersion time. The optimum water stability for SSPA was attained at 4 days. The water stability of SSPA was generally excellent under short-term high-temperature or medium-temperature H_2O immersion, but significantly deceased after long periods of high-temperature H_2O-immersion schemes.
- The SEM results showed that under short-term, high-temperature H_2O-immersion conditions, the interfacial phase of asphalt and steel slag was generally continuous and uniform; that is, the steel slag aggregates and asphalt contact had a firm mechanical bonding force that enhanced the interfacial strength between the asphalt and steel slag aggregates. The change in the spacing size of the ITZ reflected the chemical adhesion mechanism between the asphalt and steel slag aggregates.
- The FTIR results showed that there was a chemical bonding reaction between the asphalt and steel slag aggregates. This inherently enhanced the adhesion properties between the asphalt and steel slag aggregates; however, the combination of long-time and high-temperature H_2O-immersion severely weakened the adhesive bonding between the asphalt and steel slag aggregates.
- The XRD results showed that with an increase in the H_2O immersion time, the crystallization peak of $CaCO_3$ produced via the hydration reaction of steel slag appeared to be significantly enhanced. Furthermore, the $CaSO_4 \cdot 2H_2O$ formed via the chemical reaction of various acidic groups contained in asphalt and the $CaCO_3$ can enhance the water stability of SSPA.

In this paper, the influence of the adhesion mechanism between the asphalt and steel slag aggregates on the water stability of SSPA was chemically and quantitatively analyzed. For a country like China that is heavily involved in steel making, this study can environmentally promote and accelerate the resource utilization of waste steel slag, while for the industry, this study can valuably provide technical credence and reference data for the construction of permeable-surfaced roads using SSPA. However, the influence of asphalt aging and steel slag aging on the water stability of SSPA has not been thoroughly analyzed in this paper. In the future, it is necessary to study the change law of asphalt aging performance and steel slag aging performance under a high-temperature and high-humidity environment, and comprehensively analyze the influence of various factors on the water stability of SSPA.

Author Contributions: Conceptualization, X.C., M.Z. and W.W.; methodology, M.Z. and W.W.; validation, J.Y. (Jinhai Yin) and Z.L.; formal analysis, M.Z. and W.W.; investigation, J.Y. (Jianming Yao); resources, X.C. and J.Y. (Jianming Yao); writing—original draft preparation, M.Z. and W.W.; writing—review and editing, X.C., X.Z., J.Y. and Z.L.; visualization, M.Z.; supervision, X.C., X.Z. and J.Y. (Jianming Yao); funding acquisition, J.Y. (Jianming Yao) and X.Z. All authors have read and agreed to the published version of the manuscript.

Funding: This research was funded by Suzhou Jiaotou Construction Management Co., Ltd. (Grant No. 8521008637 and Grant No. 8521008638) and Kunshan Communication Development Holding Group Co., Ltd. (Grant No. 8521009349).

Institutional Review Board Statement: Not applicable.

Informed Consent Statement: Not applicable.

Data Availability Statement: Not applicable.

Acknowledgments: Special thanks and due gratitude go to all those who offered their administrative and technical support during the course of this study.

Conflicts of Interest: The authors have received research grants from Suzhou Jiaotou Construction Management Co., Ltd. and Kunshan Communication Development Holding Group Co., Ltd. J.Y. is employed by Suzhou Jiaotou Construction Management Co., Ltd., and X.Z. is employed by Kunshan Communication Development Holding Group Co., Ltd.

References

1. Kutuk, S.; Kutuk-Sert, T. An examination of nanoparticle colemanite mineral added warm mix asphalt. *Constr. Build. Mater.* **2020**, *243*, 118252. [CrossRef]
2. Kütük-Sert, T.K.-S.; Günbey, R.E. Investigation of nano ulexite mineral effects on mechanical behaviour of warm mix asphalt pavements. *J. Croat. Assoc. Civ. Eng.* **2020**, *72*, 503–513.
3. Walubita, L.F.; Martinez-Arguelles, G.; Polo-Mendoza, R.; Ick-Lee, S.; Fuentes, L. Comparative Environmental Assessment of Rigid, Flexible, and Perpetual Pavements: A Case Study of Texas. *Sustainability* **2022**, *14*, 9983. [CrossRef]
4. Zhang, J.; Simate, G.S.; Hu, X.D.; Souliman, M.; Walubita, L.F. Impact of recycled asphalt materials on asphalt binder properties and rutting and cracking performance of plant-produced mixtures. *Constr. Build. Mater.* **2017**, *155*, 654–663. [CrossRef]
5. Sanchez-Cotte, E.H.; Fuentes, L.; Martinez-Arguelles, G.; Quintana, H.A.R.; Walubita, L.F.; Cantero-Durango, J.M. Influence of recycled concrete aggregates from different sources in hot mix asphalt design. *Constr. Build. Mater.* **2020**, *259*, 120427. [CrossRef]
6. Walubita, L.F.; Djebou, D.C.S.; Faruk, A.M.; Lee, S.I.; Dessouky, S.; Hu, X.D. Prospective of Societal and Environmental Benefits of Piezoelectric Technology in Road Energy Harvesting. *Sustainability* **2018**, *10*, 383. [CrossRef]
7. Li, J.; Zhang, J.; Ni, S.N.; Liu, L.B.; Walubita, L.F. Mechanical performance and environmental impacts of self-compacting concrete with recycled demolished concrete blocks. *J. Clean. Prod.* **2021**, *293*, 126129. [CrossRef]
8. Yang, X.X.; Zhou, X.T.; Kan, T.; Strezov, V.; Nelson, P.; Evans, T.; Jiang, Y.J. Characterization of size resolved atmospheric particles in the vicinity of iron and steelmaking industries in China. *Sci. Total Environ.* **2019**, *694*, 133534. [CrossRef]
9. Kılıçarslan, Z. Comparative analysis of the competitiveness in the steel sector: The case of top 10 steel-producing countries. *Erciyes Üniversitesi İktisadi Ve İdari Bilim. Fakültesi Derg.* **2021**, *60*, 755–773. [CrossRef]
10. Liu, H.M.; Li, Q.Q.; Li, G.G.; Ding, R. Life Cycle Assessment of Environmental Impact of Steelmaking Process. *Complexity* **2020**, *2020*, 8863941. [CrossRef]
11. Hainin, M.R.; Aziz, M.M.A.; Ali, Z.; Putra Jaya, R.; Elsergany, M.; Yaacob, H. Steel Slag as A Road Construction Material. *J. Teknol.* **2015**, *73*, 33–38. [CrossRef]
12. Motz, H.; Geiseler, J. Products of steel slags an opportunity to save natural resources. *Waste Manag.* **2001**, *21*, 285–293. [CrossRef]

13. Guo, J.L.; Bao, Y.P.; Wang, M. Steel slag in China: Treatment, recycling, and management. *Waste Manag.* **2018**, *78*, 318–330. [CrossRef] [PubMed]
14. Yi, H.; Xu, G.P.; Cheng, H.G.; Wang, J.S.; Wan, Y.F.; Chen, H. An overview of utilization of steel slag. In Proceedings of the 7th International Conference on Waste Management and Technology (ICWMT), Beijing, China, 5–7 September 2012; pp. 791–801.
15. Liu, W.H.; Li, H.; Zhu, H.M.; Xu, P.J. The Interfacial Adhesion Performance and Mechanism of a Modified Asphalt-Steel Slag Aggregate. *Materials* **2020**, *13*, 1180. [CrossRef] [PubMed]
16. de Moura, B.L.R.; Teixeira, J.; Simao, R.A.; Khedmati, M.; Kim, Y.R.; Pires, P.J.M. Adhesion between steel slag aggregates and bituminous binder based on surface characteristics and mixture moisture resistance. *Constr. Build. Mater.* **2020**, *264*, 120685. [CrossRef]
17. Wang, W.Z.; Shen, A.Q.; He, Z.M.; Liu, H.C. Evaluation of the adhesion property and moisture stability of rubber modified asphalt mixture incorporating waste steel slag. *J. Adhes. Sci. Technol.* **2023**, *37*, 296–318. [CrossRef]
18. Zalnezhad, M.; Hesami, E. Effect of steel slag aggregate and bitumen emulsion types on the performance of microsurfacing mixture. *J. Traffic Transp. Eng. Engl. Ed.* **2020**, *7*, 215–226. [CrossRef]
19. Walubita, L.F.; Martin, A.E.; Jung, S.H.; Glover, C.J.; Park, E.S.; Chowdhury, A.R.; Lytton, R.L. *Comparison of Fatigue Analysis Approaches for Two Hot Mix Asphalt Concrete (HMAC) Mixtures*; Texas A&M Transportation Institute: Bryan, TX, USA, 2005.
20. Gan, Y.W.; Li, C.M.; Ke, W.; Deng, Q.H.; Yu, T. Study on pavement performance of steel slag asphalt mixture based on surface treatment. *Case Stud. Constr. Mater.* **2022**, *16*, e01131. [CrossRef]
21. Yang, C.; Wu, S.; Cui, P.; Amirkhanian, S.; Zhao, Z.; Wang, F.; Zhang, L.; Wei, M.; Zhou, X.; Xie, J. Performance characterization and enhancement mechanism of recycled asphalt mixtures involving high RAP content and steel slag. *J. Clean. Prod.* **2022**, *336*, 130484. [CrossRef]
22. Cui, P.; Wu, S.; Xiao, Y.; Hu, R.; Yang, T. Environmental performance and functional analysis of chip seals with recycled basic oxygen furnace slag as aggregate. *J. Hazard. Mater.* **2021**, *405*, 124441. [CrossRef]
23. Liu, J.Z.; Xu, J.; Liu, Q.; Wang, S.Y.; Yu, B. Steel Slag for Roadway Construction: A Review of Material Characteristics and Application Mechanisms. *J. Mater. Civ. Eng.* **2022**, *34*, 03122001. [CrossRef]
24. Alvarez, A.E.; Fernandez, E.M.; Martin, A.E.; Reyes, O.J.; Simate, G.S.; Walubita, L.F. Comparison of permeable friction course mixtures fabricated using asphalt rubber and performance-grade asphalt binders. *Constr. Build. Mater.* **2012**, *28*, 427–436. [CrossRef]
25. Walubita, L.F.; Lee, S.I.; Faruk, A.N.M.; Scullion, T.; Nazarian, S.; Abdallah, I. *Texas Flexible Pavements and Overlays: Year 5 Report—Complete Data Documentation*; Texas A&M Transportation Institute: Bryan, TX, USA, 2017.
26. Walubita, L.F.; Scullion, T.; Leidy, J.; Liu, W.T. Non-Destructive Testing Technologies Application of the Ground Penetrating Radar (GPR) to Perpetual Pavements. *Road Mater. Pavement Des.* **2009**, *10*, 259–286. [CrossRef]
27. Zevenbergen, C.; Fu, D.F.; Pathirana, A. Transitioning to Sponge Cities: Challenges and Opportunities to Address Urban Water Problems in China. *Water* **2018**, *10*, 1230. [CrossRef]
28. Sha, A.; Liu, Z.; Jiang, W.; Qi, L.; Hu, L.; Jiao, W.; Barbieri, D.M. Advances and development trends in eco-friendly pavements. *J. Road Eng.* **2021**, *1*, 1–42. [CrossRef]
29. Qin, Z.; Yao, Y.J.; Zhao, J.W.; Fu, H.L.; Zhang, S.; Qiu, L.Y. Investigation of migration rule of rainwater for sponge city roads under different rainfall intensities. *Environ. Geochem. Health* **2022**, *44*, 3395–3407. [CrossRef]
30. Zhang, L.; Lu, Q.; Ding, Y.F.; Peng, P.; Yao, Y. Design and Performance Simulation of Road Bioretention Media for Sponge Cities. *J. Perform. Constr. Facil.* **2018**, *32*, 04018061. [CrossRef]
31. Guan, X.; Wang, J.Y.; Xiao, F.P. Sponge city strategy and application of pavement materials in sponge city. *J. Clean. Prod.* **2021**, *303*, 127022. [CrossRef]
32. Liu, W.H.; Li, H.; Zhu, H.M.; Xu, P.J. Properties of a Steel Slag-Permeable Asphalt Mixture and the Reaction of the Steel Slag-Asphalt Interface. *Materials* **2019**, *12*, 3603. [CrossRef]
33. Walubita, L.F.; Faruk, A.N.M.; Zhang, J.; Hu, X.D.; Lee, S.I. The Hamburg rutting test—Effects of HMA sample sitting time and test temperature variation. *Constr. Build. Mater.* **2016**, *108*, 22–28. [CrossRef]
34. Chen, Z.W.; Gong, Z.L.; Jiao, Y.Y.; Wang, Y.; Shi, K.; Wu, J.C. Moisture stability improvement of asphalt mixture considering the surface characteristics of steel slag coarse aggregate. *Constr. Build. Mater.* **2020**, *251*. [CrossRef]
35. Liang, Y.C.; Bai, T.; Zhou, X.L.; Wu, F.; Chenxin, C.; Peng, C.; Fuentes, L.; Walubita, L.F.; Li, W.; Wang, X.C. Assessing the Effects of Different Fillers and Moisture on Asphalt Mixtures' Mechanical Properties and Performance. *Coatings* **2023**, *13*, 288. [CrossRef]
36. Walubita, L.F.; Hugo, F.; Martin, A.E. Indirect tensile fatigue performance of asphalt after MMLS3 trafficking under different environmental conditions. *J. Van Die Suid-Afr. Inst. Van Siviele Ingenieurswese* **2002**, *44*, 2–11.
37. Liu, H.B.; Zhu, B.; Wei, H.B.; Chai, C.; Chen, Y. Laboratory Evaluation on the Performance of Porous Asphalt Mixture with Steel Slag for Seasonal Frozen Regions. *Sustainability* **2019**, *11*, 6924. [CrossRef]
38. Liu, Y.W.; Apeagyei, A.; Ahmad, N.; Grenfell, J.; Airey, G. Examination of moisture sensitivity of aggregate-bitumen bonding strength using loose asphalt mixture and physico-chemical surface energy property tests. *Int. J. Pavement Eng.* **2014**, *15*, 657–670. [CrossRef]
39. Walubita, L.F. Comparison of Fatigue Analysis Approaches for Predicting Fatigue Lives of Hot-Mix Asphalt Concrete (HMAC) Mixtures. Doctoral Dissertation, Texas A&M University, Bryan, TX, USA, 2006.

40. Xu, F.; Nie, X.; Gan, W.X.; Hongzhi, E.; Xu, P.Y.; Cao, H.Q.; Gong, R.F.; Zhang, Y.X. Moisture Sensitivity Evaluation of the Asphalt Mortar-Aggregate Filler Interface Using Pull-Out Testing and 3-D Structural Imaging. *Coatings* **2023**, *13*, 868. [CrossRef]
41. Walubita, L.F.; Martin, A.E.; Cleveland, G.S.; Lytton, R.L. Computation of pseudo strain energy and Paris law fracture coefficients from surface energy and uniaxial strain-controlled tension test data. *Int. J. Pavement Eng.* **2006**, *7*, 167–178. [CrossRef]
42. Hu, X.D.; Jiang, M.; Bai, T.; Pan, P.; Walubita, L.F. Development and validation of an enhanced test setup for assessing HMA stripping potential under hydrodynamic pressure. *Road Mater. Pavement Des.* **2020**, *21*, 2024–2039. [CrossRef]
43. Mabui, D.S.; Tjaronge, M.W.; Adisasmita, S.A.; Pasra, M. Resistance to cohesion loss in cantabro test on specimens of porous asphalt containing modificated asbuton. In Proceedings of the 3rd International Conference on Civil and Environmental Engineering (ICCEE), Bali, Indonesia, 29–30 August 2019.
44. Cox, B.C.; Smith, B.T.; Howard, I.L.; James, R.S. State of Knowledge for Cantabro Testing of Dense Graded Asphalt. *J. Mater. Civ. Eng.* **2017**, *29*, 04017174. [CrossRef]
45. Mirhosseini, A.F.; Tahami, A.; Hoff, I.; Dessouky, S.; Kavussi, A.; Fuentes, L.; Walubita, L.F. Performance Characterization of Warm-Mix Asphalt Containing High Reclaimed-Asphalt Pavement with Bio-Oil Rejuvenator. *J. Mater. Civ. Eng.* **2020**, *32*, 04020382. [CrossRef]
46. Do, T.C.; Tran, V.P.; Le, V.P.; Lee, H.J.; Kim, W.J. Mechanical characteristics of tensile strength ratio method compared to other parameters used for moisture susceptibility evaluation of asphalt mixtures. *J. Traffic Transp. Eng. -Engl. Ed.* **2019**, *6*, 621–630. [CrossRef]
47. Bai, T.; Hu, Z.A.; Hu, X.D.; Liu, Y.; Fuentes, L.; Walubita, L.F. Rejuvenation of short-term aged asphalt-binder using waste engine oil. *Can. J. Civ. Eng.* **2020**, *47*, 822–832. [CrossRef]
48. Polo-Mendoza, R.; Martinez-Arguelles, G.; Walubita, L.F.; Moreno-Navarro, F.; Giustozzi, F.; Fuentes, L.; Navarro-Donado, T. Ultraviolet ageing of bituminous materials: A comprehensive literature review from 2011 to 2022. *Constr. Build. Mater.* **2022**, *350*, 128889. [CrossRef]
49. Mubaraki, M. The Effect of Modified Asphalt Binders by Fourier Transform Infrared Spectroscopy, X-ray Diffraction, and Scanning Electron Microscopy. *J. Mater. Eng. Struct.* **2019**, *6*, 5–14.
50. Zhang, Y.; Gu, Q.L.; Kang, A.H.; Ding, X.H.; Ma, T. Characterization of mesoscale fracture damage of asphalt mixtures with basalt fiber by environmental scanning electron microscopy. *Constr. Build. Mater.* **2022**, *344*, 128889. [CrossRef]
51. Application of Nano-Technology in Pavement Engineering: A Literature Review. Application of Nanotechnology in Pavements, Geological Disasters, and Foundation Settlement Control Technology. In Proceedings of the Geo-Hubei 2014 International Conference on Sustainable Civil Infrastructure, Yichang, China, 20–22 July 2014; pp. 9–16.
52. Wang, P.; Dong, Z.J.; Tan, Y.Q.; Liu, Z.Y. Identifying the rheological properties of polymer-modified bitumen based on its morphology. *Road Mater. Pavement Des.* **2017**, *18*, 249–258. [CrossRef]
53. Zhang, X.R.; Wang, J.T.; Zhou, X.X.; Zhang, Z.Q.; Chen, X.B. Mechanical Properties of the Interfacial Bond between Asphalt-Binder and Aggregates under Different Aging Conditions. *Materials* **2021**, *14*, 1221. [CrossRef]
54. *JTG E20-2011*; Standard Test Methods of Bitumen and Bituminous Mixtures for Highway Engineering. China Communications Press: Beijing, China, 2011.
55. *JTG F40-2004*; Technical Specification for Construction of Highway Asphalt Pavements. China Communications Press: Beijing, China, 2004.
56. *GB/T 24766-2009*; Steel Slag for Pervious Asphalt Pave. China Communications Press: Beijing, China, 2009.
57. *JTG/T 3350-03—2020*; Technical Specifications for Design and Construction of Porous Asphalt Pavement. China Communications Press: Beijing, China, 2020.
58. *JT/T 860.2-2013*; Modifier for Asphalt Mixture (Part 2: High Viscosity Additive). China Communications Press: Beijing, China, 2013.
59. *JT/T 533-2020*; Fiber for Asphalt Pavements. China Communications Press: Beijing, China, 2020.
60. Zhang, J.P.; Liu, G.Q.; Zhu, C.Z.; Pei, J.Z. Evaluation indices of asphalt-filler interaction ability and the filler critical volume fraction based on the complex modulus. *Road Mater. Pavement Des.* **2017**, *18*, 1338–1352. [CrossRef]
61. *CJJ/T 190-2012*; Technical Specification for Permeable Asphalt Pavement. China Communications Press: Beijing, China, 2012.
62. Walubita, L.F.; Fuentes, L.; Lee, S.I.; Dawd, I.; Mahmoud, E. Comparative evaluation of five HMA rutting-related laboratory test methods relative to field performance data: DM, FN, RLPD, SPST, and HWTT. *Constr. Build. Mater.* **2019**, *215*, 737–753. [CrossRef]
63. Holleran, I.; Wilson, D.J.; Holleran, G.; Walubita, L.; James, B. Porous Asphalt—More Than Just Safety. In Proceedings of the 2016 IPENZ Transportation Group Conference: Design, Innovation, Technology, Auckland, New Zealand, 22–24 March 2016.
64. Gao, Y.; Huang, X.M.; Yu, W.B. The Compaction Characteristics of Hot Mixed Asphalt Mixtures. *J. Wuhan Univ. Technol. Mater. Sci. Ed.* **2014**, *29*, 956–959. [CrossRef]
65. Jiang, W.; Sha, A.; Pei, J.Z.; Chen, S.; Zhou, H. Study on the fatigue characteristic of porous asphalt concrete. *Jianzhu Cailiao Xuebao/J. Build. Mater.* **2012**, *15*, 513–517+543. [CrossRef]
66. Xu, F.; Chan, T.; Luo, M. Different changes in dry and humid heat waves over China. *Int. J. Climatol.* **2020**, *41*, 1369–1382. [CrossRef]
67. Tschegg Elmar, K.; Kroyer, G.; Tan, D.-M.; Stanzl-Tschegg Stefanie, E.; Litzka, J. Investigation of Bonding between Asphalt Layers on Road Construction. *J. Transp. Eng.* **1995**, *121*, 309–316. [CrossRef]

68. Lu, Z.; Feng, Z.-g.; Yao, D.; Li, X.; Jiao, X.; Zheng, K. Bonding performance between ultra-high performance concrete and asphalt pavement layer. *Constr. Build. Mater.* **2021**, *312*, 125375. [CrossRef]
69. Mohammed, A.; Abdullah, A. Scanning Electron Microscopy (SEM): A Review. In Proceedings of the 2018 International Conference on Hydraulics and Pneumatics–HERVEX, Baile Govora, Romania, 13–15 November 2019.
70. Lamontagne, J.; Dumas, P.; Mouillet, V.; Kister, J. Comparison by Fourier transform infrared (FTIR) spectroscopy of different ageing techniques: Application to road bitumens. *Fuel* **2001**, *80*, 483–488. [CrossRef]
71. Souliman, M.I.; Gc, H.; Isied, M.; Walubita, L.F.; Sousa, J.; Bastola, N.R. Mechanistic analysis and cost-effectiveness evaluation of asphalt rubber mixtures. *Road Mater. Pavement Des.* **2020**, *21*, S76–S90. [CrossRef]
72. Li, Z.Y.; Li, R.L.; Li, C.L.; Wang, K.R.; Fan, J.Y.; Gu, R. Identification of Tibetan Medicine Zhaxun by Infrared Spectroscopy Combined With Chemometrics. *Spectrosc. Spectr. Anal.* **2023**, *43*, 526–532. [CrossRef]
73. Epp, J. X-ray diffraction (XRD) Techniques for Materials Characterization. In *Materials Characterization Using Nondestructive Evaluation (NDE) Methods*; Hübschen, G., Altpeter, I., Tschuncky, R., Herrmann, H.-G., Eds.; Woodhead Publishing: Cambridge, UK, 2016; pp. 81–124.
74. Li, Z.T.; Wang, C.B. Multi-scale Ag/CuO Photothermal Materials: Preparation and Application in Seawater Desalination. *Chin. J. Inorg. Chem.* **2020**, *36*, 1457–1464. [CrossRef]
75. Zhou, L.; Huang, W.; Lu, Q.; Zheng, M. Effects of Various Modifiers on the Bond Property and Moisture Damage Resistance of Asphalt. *J. Build. Mater.* **2021**, *24*, 377–384. [CrossRef]
76. Bagampadde, U.; Isacsson, U.; Kiggundu, B.M. Classical and Contemporary Aspects of Stripping in Bituminous Mixes. *Road Mater. Pavement Des.* **2004**, *5*, 7–43. [CrossRef]
77. Alnadish, A.M.; Aman, M.Y.; Katman, H.Y.B.; Ibrahim, M.R. Laboratory assessment of the performance and elastic behavior of asphalt mixtures containing steel slag aggregate and synthetic fibers. *Int. J. Pavement Res. Technol.* **2021**, *14*, 473–481. [CrossRef]
78. Zhou, X.X.; Zhao, G.Y.; Tighe, S.; Chen, M.Z.; Wu, S.P.; Adhikari, S.; Gao, Y.M. Quantitative comparison of surface and interface adhesive properties of fine aggregate asphalt mixtures composed of basalt, steel slag, and andesite. *Constr. Build. Mater.* **2020**, *246*, 473–481. [CrossRef]
79. Mi, G.; Qiang, W.; Wang, W. Destructive effect of steel slag coarse aggregate on the concrete under autoclaved condition. *J. Tsinghua Univ.* **2015**, *55*, 940–944.
80. Liu, J.; Yu, B.; Hong, Q. Molecular dynamics simulation of distribution and adhesion of asphalt components on steel slag. *Constr. Build. Mater.* **2020**, *255*, 119332. [CrossRef]
81. Shen, A.; Zhai, C.; Guo, Y.; Yang, X. Mechanism of adhesion property between steel slag aggregate and rubber asphalt. *J. Adhes. Sci. Technol.* **2018**, *32*, 2727–2740. [CrossRef]
82. Chen, X.; Wen, W.; Zhou, J.; Zhou, X.; Ning, Y.; Liang, Z.; Ma, Z. Research on the Interaction Capability and Microscopic Interfacial Mechanism between Asphalt-Binder and Steel Slag Aggregate-Filler. *Coatings* **2022**, *12*, 1871. [CrossRef]
83. Kutuk-Sert, T.; Ozturk, M.; Kutuk, S. Digital image processing of warm mix asphalt enriched with nanocolemanite and nanoulexite minerals. *Constr. Build. Mater.* **2023**, *399*, 132542. [CrossRef]
84. Kara, C.; Kutuk, S.; Kutuk-Sert, T. Improvement of the durability of concrete by substitution of raw ground colemanite. *Case Stud. Constr. Mater.* **2023**, *19*, e02393. [CrossRef]
85. Bai, T.; Cheng, Z.; Hu, X.D.; Fuentes, L.; Walubita, L.F. Viscoelastic modelling of an asphalt pavement based on actual tire-pavement contact pressure. *Road Mater. Pavement Des.* **2021**, *22*, 2458–2477. [CrossRef]
86. Walubita, L.F.; Zhang, J.; Das, G.; Hu, X.D.; Mushota, C.; Alvarez, A.E.; Scullion, T. Hot-Mix Asphalt Permanent Deformation Evaluated by Hamburg Wheel Tracking, Dynamic Modulus, and Repeated Load Tests. *Transp. Res. Rec.* **2012**, *22*, 2458–2477. [CrossRef]
87. Ling, M.; Lee, S.I.; Ji, J.; Fuentes, L.; Walubita, L.F. Assessing permanent deformation potential of asphalt mixtures based on viscoelastic characteristics. *Int. J. Pavement Eng.* **2023**, *24*, 2240472. [CrossRef]
88. Chen, F.H.; Zhang, D.F.; Liu, G.; Huang, J.F.; Wu, S. Experimental investigation of improving anti-stripping performance of asphalt mixture. *J. Wuhan Univ. Technol.* **2007**, *29*, 9–11.
89. Jonczy, I.; Grzesik, B. Polymorphic transformations of dicalcium silicates in steel slags used in the production of road aggregates. *Gospod. Surowcami Miner. Miner. Resour. Manag.* **2021**, *37*, 97–116. [CrossRef]
90. Feng, X.; Zhao, M.; Chen, W.; Xie, M. Research of Road Performances and Microcosmic Mechanisms of Coal Waste Powder Asphalt Mortar. *J. Build. Mater.* **2019**, *22*, 113–119. [CrossRef]
91. Yao, H.; Dai, Q.L.; You, Z.P. Fourier Transform Infrared Spectroscopy characterization of aging-related properties of original and nano-modified asphalt binders. *Constr. Build. Mater.* **2015**, *101*, 1078–1087. [CrossRef]
92. Fernández-Gómez, W.D.; Rondón Quintana, H.A.; Daza, C.E.; Reyes Lizcano, F.A. The effects of environmental aging on Colombian asphalts. *Fuel* **2014**, *115*, 321–328. [CrossRef]
93. Zhang, L.; Long, N.Q.; Liu, Y.; Wang, L. Cross-scale study on the influence of moisture-temperature coupling conditions on adhesive properties of rubberized asphalt and steel slag. *Constr. Build. Mater.* **2022**, *332*, 127401. [CrossRef]
94. Liu, W.H.; Li, H.; Zhu, H.M.; Xu, P.J. Effects of Steel-Slag Components on Interfacial-Reaction Characteristics of Permeable Steel-Slag-Bitumen Mixture. *Materials* **2020**, *13*, 3885. [CrossRef]
95. Jing, W.; Jiang, J.P.; Ding, S.; Duan, P. Hydration and Microstructure of Steel Slag as Cementitious Material and Fine Aggregate in Mortar. *Molecules* **2020**, *25*, 4456. [CrossRef]

96. Li, H.; Liu, W.; Lu, J.; Lu, Y.; Shi, S.; Wang, Z.; Ye, Q.; Jia, Z. Effect of microwave-assisted acidification on the microstructure of coal: XRD, 1H-NMR, and SEM studies. *Int. J. Min. Sci. Technol.* **2023**, *33*, 919–926. [CrossRef]
97. Wang, Q.; Yan, P.Y. Hydration properties of basic oxygen furnace steel slag. *Constr. Build. Mater.* **2010**, *24*, 1134–1140. [CrossRef]
98. Wang, Q.; Yan, P.Y.; Han, S. Activity index for steel slag. *Mag. Concr. Res.* **2011**, *63*, 737–742. [CrossRef]
99. Wang, Q.A.; Yan, P.Y.; Feng, J.W. A discussion on improving hydration activity of steel slag by altering its mineral compositions. *J. Hazard. Mater.* **2011**, *186*, 1070–1075. [CrossRef] [PubMed]
100. Xin-li, L.Y.W.B.-h.N.W.M. Synergies in Early Hydration Reaction of Slag-Steel Slag-Gypsum System. *J. Northeast. Univ.* **2020**, *41*, 581–586. [CrossRef]